

# Interactions of Grid-Forming Power Converters and Synchronous Machines – A Comparative Study

Ali Tayyebi, Dominic Groß, Adolfo Anta, Friederich Kupzog and Florian Dörfler

**Abstract**—An inevitable consequence of the global power system transition towards nearly 100% renewable-based generation is the loss of conventional bulk generation by synchronous machines, their inertia, and accompanying frequency and voltage control mechanisms. This gradual transformation of the power system to a low-inertia system leads to critical challenges in maintaining system stability. Novel control techniques for converters, so-called grid-forming strategies, are expected to address these challenges and replicate functionalities that so far have been provided by synchronous machines. This article reviews existing grid-forming converter control techniques and presents a high-fidelity case study that includes grid-forming converters as well as synchronous machines. We provide a performance comparison that accounts for the interactions between synchronous machines and converters and analyze the response of various grid-forming control approaches to contingencies, i.e., large changes in load and the loss of a synchronous machine. Our case study highlights the (possibly surprising) positive impact of the grid-forming converters on frequency stability and analyzes the potential limitations of each control technique when interacting with synchronous machines. Our studies also demonstrate how and when the interaction between the fast grid-forming converter, the DC source current limitations, and the slow synchronous machine dynamics contributes to system instability.

## I. INTRODUCTION

At the heart of the energy transition is the change in generation technology; from fossil fuel based thermal generation to converter interfaced renewable generation [1]. One of the major consequences of this transition towards a nearly 100% renewable system is the gradual loss of synchronous machines (SMs), their inertia, and control mechanisms. This loss of the rotational inertia changes the nature of the power system to a low-inertia network resulting in critical stability challenges [1]–[3]. On the other hand, low-inertia power systems are characterized by large-scale integration of generation interfaced by power converters [4], allowing frequency and voltage regulation at much faster time-scales compared to SMs [1], [5].

Indeed, power converters are already starting to provide new ancillary services, modifying their active and reactive power output based on local measurements of frequency and voltage. However, because of the dependency on frequency measurements these *grid-following* control techniques only replicate the instantaneous inertial response of SMs with

a delay and perform sub-optimally on the time scales of interest [6]. To resolve this issue, *grid-forming converters* (GFCs) are envisioned to be the cornerstone of future power systems. Based on the properties and functions of SMs, it is expected that grid-forming converters must support load-sharing/drooping, black-start, inertial response, and hierarchical frequency/voltage regulation. While these services might not be necessary in a future converter-based grid, a long transition phase is expected, where SMs and GFCs must be able to interact and ensure system stability.

Several grid-forming control strategies have been proposed in recent years [5]. *Droop control* mimics the speed droop mechanism present in SMs and is a widely accepted baseline solution [7]–[9]. As a natural further step, emulation of SM dynamics and control led to so-called *virtual synchronous machine* (VSM) strategies [10]–[13]. Recently, *matching control* strategies that exploit structural similarities of converters and synchronous machine and *match* their dynamic behavior have been proposed [14]–[17]. In contrast, virtual oscillator control (VOC) uses GFCs to mimic the synchronizing behavior of Liénard-type oscillators and can globally synchronize a converter-based power system [18], [19]. However, the nominal power injection of VOC cannot be specified. This limitation is overcome by *dispatchable virtual oscillator control* (dVOC) [20]–[22] that ensures synchronization to a pre-specified operating point that satisfies the AC power flow equations. Lastly, communication based strategies underpinned by IoT/ICT utilization have been proposed [23]. In this manuscript, we restrict our focus to decentralized techniques (i.e., only requiring infrequent communication for dispatch) that are resilient to communication failures and compatible with today’s power system operation.

In this article we provide an extended review on decentralized grid-forming control techniques and introduce suitable high-fidelity converter and machine models for studying their interactions in an electromagnetic transients (EMT) simulation of the IEEE 9-bus test system. We explicitly consider the dynamics of the converter DC-link capacitor, the response time of the DC power source, and its current limits. Moreover, we combine four different grid-forming control strategies with standard cascaded inner control loops for the AC current and AC voltage [24]. We compare various performance aspects of grid-forming control techniques, namely: 1) their impact on frequency performance metrics e.g., nadir and rate of change of frequency (RoCoF), 2) their interaction with synchronous machines, 3) their response under large load disturbance magnitudes, and 4) their response to loss of synchronous machine. This comparative study highlights the positive impact

This work was partially funded by the independent research fund of the the power system digitalization group at the Electric Energy Systems (EES) competence unit of the Austrian Institute for Technology (AIT) and ETH Zürich funds. A. Tayyebi is with AIT, 1210 Vienna, Austria, and also with the Automatic Control Laboratory, ETH Zürich, Switzerland. A. Anta and F. Kupzog are with AIT, 1210 Vienna, Austria. D. Groß, and F. Dörfler are with the Automatic Control Laboratory, ETH Zürich, 8092 Zürich, Switzerland; Email: {ali.tayyebi-khameneh,adolfo.anta,friederich.kupzog}@ait.ac.at, {grodo,dorfler}@ethz.ch.

of grid-forming control techniques on improving standard power system performance metrics. Moreover, we observe that limiting the maximum output current of the DC source accompanied by the interaction of fast converters and slow synchronous machine dynamics can destabilize VSMs, droop control, and dVOC, while matching control appears to be unaffected.

## II. MODEL DESCRIPTION

Throughout this study, we use a test system comprised of power converters and synchronous machines. This section describes the models of the individual devices and components.

### A. Two-level Voltage Source Converter Model

We use a standard average-switch model of the two-level voltage source converter shown in Figure 1 (see, e.g., [16])

$$C_{dc}\dot{v}_{dc} = i_{dc} - G_{dc}v_{dc} - i_x, \quad (1a)$$

$$L\dot{i}_s = v_s - Ri_s - v, \quad (1b)$$

$$C\dot{v} = i_s - i, \quad (1c)$$

where  $C_{dc}$  denotes the DC-link capacitance,  $G_{dc}$  denotes the conductance which models DC losses, and,  $L$ ,  $C$ , and  $R$  denote filter inductance, capacitance, and resistance. Moreover,  $v_{dc}$  represents the DC voltage,  $i_{dc}$  is the current flowing out of the controllable DC current source,  $m$  denotes the modulation signal of the full-bridge averaged switching stage model,  $i_x = (1/2)m^T i_s$  denotes the net DC current delivered to the switching stage, and  $i_s$  and  $v_s = (1/2)mv_{dc}$  respectively are the AC switching node current and voltage (i.e., before the output filter), and  $i$  and  $v$  are the output current and voltage. To obtain a more realistic model of the energy source, we model its response time by a first order system

$$\tau_{dc}\dot{i}_{dc} = i_{dc}^* - i_{dc}, \quad (2)$$

where  $i_{dc}^*$  is the DC current reference,  $\tau_{dc}$  is the DC source time constant, and  $i_{dc}$  denotes the current provided by the DC source. Moreover, the DC source current limitation is modeled by the saturation function

$$i_{dc} = \text{sat}(i_{dc}^*) = \begin{cases} i_{dc}^* & \text{if } |i_{dc}^*| < |i_{dc}^{\max}|, \\ \text{sgn}(i_{dc}^*)i_{dc}^{\max} & \text{if } |i_{dc}^*| \geq |i_{dc}^{\max}|, \end{cases} \quad (3)$$

where  $i_{dc}^{\max}$  is the maximum DC source current.

In this work, (1)–(3) represent a structure-preserving reduced-order model of a high power large-scale converter system which follows a modular design. For such a system, a module consists of multiple AC-coupled converters rated at a few hundred kVA interfaced by an LV/MV transformer at the distribution level. Consequently, clusters of these modules are coupled at the medium voltage level and interfaced to the transmission system by a single MV/HV transformer. Figure

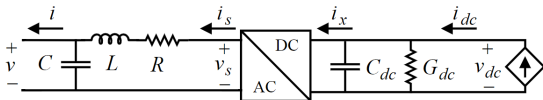


Fig. 1: Converter model single line diagram.

2 illustrates the modeling for two converters per module and  $n$  modules in total. In order to approximate the parameters of the reduced-order model (1) of the modular system shown in Figure 2 we adopt the scaling laws proposed in [25]

$$G_{dc} = 2ng_{dc}, \quad C_{dc} = 2nc_{dc}, \quad R = \frac{r}{2n}, \quad L = \frac{l}{2n}, \quad C = 2nc,$$

where  $g_{dc}$ ,  $c_{dc}$ ,  $r$ ,  $l$  and  $c$  denote the parameters of the identical converters for an individual module. The reduced order LV/MV transformer model is scaled accordingly. A similar analysis as the one in [25] must be done for each grid-forming control strategy to ensure that the reduced-order model adequately represents the dynamics of a whole module. The formal analysis is out of the scope of this paper and will be reported in future works.

### B. Synchronous Machine Model

In this work we adopt a high-fidelity 8th order synchronous machine model from Sim Power System Matlab/Simulink library that consists of six electrical states (stator, field winding, and damper windings), and two mechanical states [3], [26]. We further augment the system with a ST1A type excitation dynamics with built-in automatic voltage regulator (AVR) [27]. To counteract the well-known destabilizing effect of the AVR on the synchronizing torque, we equip the system with a simplified power system stabilizer comprised of a two-stage lead-lag compensator [3, Sec. 12.5]. Lastly, the governor and turbine dynamics are respectively modeled by proportional speed droop control and a first order system

$$p = p^* + d_p(\omega^* - \omega), \quad (4a)$$

$$\tau_g \dot{p} = p - p_\tau, \quad (4b)$$

where  $p^*$  denotes the power set-point,  $p$  is the governor output,  $d_p$  denotes the droop gain, and  $\omega^*$  and  $\omega$  denote nominal and measured frequency, respectively. Furthermore,  $\tau_g$  is the turbine time constant and  $p_\tau$  is the turbine output power.

### C. Network Model

To study transmission level dynamics of a low-inertia power system, we use Sim Power Systems to perform an EMT simulation of the IEEE 9-bus test system shown in Figure 3 [28]. We assume that the system is symmetric and balanced, model the lines via nominal  $\pi$  sections, i.e., considering RLC line dynamics, model the transformers via three-phase linear transformer models, and consider constant impedance loads. We emphasize that the line dynamics cannot be neglected in the presence of grid-forming converters due to potential adverse interactions between their fast response and the line dynamics [21], [29], [30].

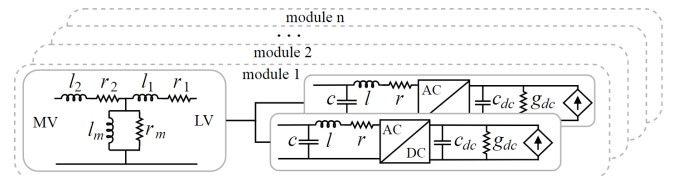


Fig. 2: Modular large-scale converter system.

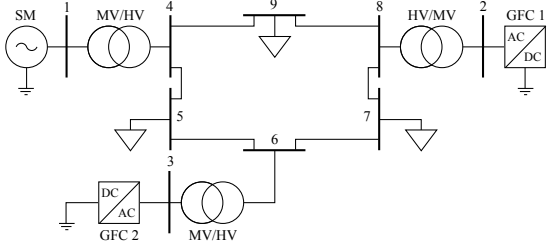


Fig. 3: IEEE 9-bus system with large-scale converter systems.

### III. GRID-FORMING CONTROL ARCHITECTURES

In this section we briefly review the standard cascaded voltage and current control architecture for two-level voltage source converters that tracks a voltage reference provided by a reference model (e.g., droop control). Moreover, we propose a controller for the converter DC voltage. Subsequently, we review four common grid-forming control strategies that provide a voltage reference to the inner voltage control loop. For each strategy, we describe the angle dynamics, frequency dynamics and AC voltage magnitude regulation.

#### A. Cascaded AC Voltage and AC Current Control

We employ a standard converter control architecture that consists of a reference model providing a reference voltage  $\hat{v}$  with angle  $\angle \hat{v} = \theta$  and magnitude  $\|\hat{v}\|$ . The modulation signal  $m$  is determined by cascaded proportional-integral (PI) controllers that are implemented in  $dq$ -coordinates (rotating with the reference angle  $\theta$ ) and track the voltage reference  $\hat{v}$  (see [24]). The voltage tracking error  $\hat{v} - v$  is used to compute the reference  $i_s^* = [i_{sd}^* \ i_{sq}^*]^T$  for the switching node current  $i_s$

$$\dot{x}_v = \hat{v} - v, \quad (5a)$$

$$i_s^* = i + C\omega J_2 v + K_{pv}(\hat{v} - v) + K_{iv}x_v. \quad (5b)$$

Here  $x_v = [x_{vd} \ x_{vq}]^T$  denotes the integrator state,  $v = [v_d \ v_q]^T$  denotes the output voltage measurement,  $\hat{v} = [\hat{v}_d \ 0]^T$  denotes the reference voltage,  $i = [i_d \ i_q]^T$  denotes the output current,  $J_2 = \begin{bmatrix} 0 & -1 \\ 1 & 0 \end{bmatrix}$  denotes the rotation matrix by  $\pi/2$ ,  $I_2$  denotes the two-dimensional identity matrix, and  $K_{pv} = k_{pv}I_2$  and  $K_{iv} = k_{iv}I_2$  denote the diagonal matrices of proportional and integral gains, respectively. Next, a PI controller for the current  $i_s = [i_{sd} \ i_{sq}]^T$  is used to track  $i_s^*$

$$\dot{x}_i = i_s^* - i_s, \quad (6a)$$

$$v_s^* = v + (L\omega J_2 + RI_2)i_s + K_{pi}(i_s^* - i_s) + K_{ii}x_i, \quad (6b)$$

where  $x_i = [x_{id} \ x_{iq}]^T$  denotes the integrator state, and  $K_{pi} = k_{pi}I_2$  and  $K_{ii} = k_{ii}I_2$  denote the diagonal matrices of proportional and integral gains, respectively. Note that the first two terms of the right hand side of equations defining  $i_s^*$  and  $v_s^*$  in (5) and (6) are feed-forward terms. Finally, the three-phase modulation signal is given by  $m = 2v_s^*/v_{dc}^*$ .

#### B. DC Voltage Control

The DC current reference  $i_{dc}^*$  tracked by the controllable DC source (2) is given by a proportional control for the DC voltage

and feed-forward terms based on the nominal AC active power injection  $p^*$  and the filter losses

$$i_{dc}^* = k_{dc}(v_{dc}^* - v_{dc}) + G_{dc}v_{dc} + \frac{p^*}{v_{dc}^*} + \frac{(v_{dc}i_x - p)}{v_{dc}^*}, \quad (7)$$

where  $v_{dc}i_x$  is the DC power flowing into the switches,  $p$  is the AC power injected into the system, and the last term on the right hand side of (7) implements a feed-forward power control that compensates the filter losses. The loss compensation is required to ensure exact tracking of the power reference by matching control (see Section III-E) and also improves the DC voltage regulation for the other control strategies considered in this study. Thus, to ensure a fair comparison, we apply (7) for all control strategies discussed throughout this work.

#### C. Droop Control

Droop control resembles the speed droop property (4a) of the SM governor [7]–[9] and trades off deviations of the power injection (from its nominal value  $p^*$ ) and frequency deviations (from its nominal value  $\omega^*$ )

$$\dot{\theta} = \omega, \quad (8a)$$

$$\omega = \omega^* + d_\omega(p^* - p), \quad (8b)$$

where  $d_\omega$  denotes the droop gain. To replicate the service provided by the automatic voltage regulator (AVR) of synchronous machines we use a PI controller acting on the output voltage error

$$\hat{v}_d = k_p(v^* - v) + k_i \int_0^t (v^* - v(\tau)) d\tau \quad (9)$$

to obtain the direct axis reference  $\hat{v}_d$  for the underlying voltage loop ( $v^*$  and  $v$  are the reference and measured voltage magnitude). We remark that the reactive power injection varies such that exact voltage regulation is achieved.

#### D. Virtual Synchronous Machine

Many variations of virtual synchronous machines (VSMs) have been proposed [10]–[12]. In this work, we consider the frequency dynamics induced by the synchronverter [12]

$$\dot{\theta} = \omega, \quad (10a)$$

$$\ddot{\theta} = \frac{D_p}{J}(\omega^* - \omega) + \frac{1}{J\omega^*}(p^* - p), \quad (10b)$$

where  $D_p$  and  $J$  are the virtual damping and inertia constants. Note that the dynamics (10) reduce to droop control (8) when using  $J/D_p \approx 0$  as recommended in [12]. These angle dynamics capture the main salient features of virtual synchronous machines, but do not suffer from drawbacks of more complicated implementations (see [5] for a discussion). The three-phase voltage induced by the VSM is given by

$$\hat{v} = 2\omega M_f i_f \left[ \sin(\theta) \quad \sin(\theta - \frac{2\pi}{3}) \quad \sin(\theta - \frac{4\pi}{3}) \right]^T, \quad (11)$$

where  $M_f$  and  $i_f$  are respectively the virtual mutual inductance magnitude and excitation current. Similar to (9), we utilize input  $i_f$  to achieve exact AC voltage regulation via PI control and thereby replicate the function of the AVR of a synchronous machine

$$i_f = \frac{k_p}{M_f}(v^* - v) + \frac{k_i}{M_f} \int_0^t (v^* - v(\tau)) d\tau. \quad (12)$$

### E. Matching Control

Matching control is a grid-forming control strategy that exploits structural similarities between power converters and SMs [14]–[17] and is based on the observation that the DC link voltage - similar to the synchronous machine frequency - indicates power imbalances. Hence the DC voltage, up to a constant factor, is used to drive the converter frequency. Furthermore, analogous to the machine input torque, the DC current is used to control the AC power injection. The angle dynamics of matching control are represented by

$$\dot{\theta} = \omega = k_{\theta} v_{dc}, \quad (13)$$

where  $k_{\theta} := \omega^*/v_{dc}^*$ . Finally, the AC voltage magnitude is controlled through the modulation magnitude  $\mu$  by a PI controller

$$\mu = k_p(v^* - v) + k_i \int_0^t (v^* - v(\tau)) d\tau. \quad (14)$$

The reference voltage angle and magnitude for the voltage controller in  $dq$ -coordinates is given by  $\theta$  and  $\hat{v}_d = \mu$ .

### F. Dispatchable Virtual Oscillator Control

Dispatchable virtual oscillator control (dVOC) [20]–[22] is a decentralized grid-forming control strategy that guarantees almost global asymptotic stability for interconnected GFCs with respect to nominal voltage and power set-points [20], [21]. The analytic stability conditions for dVOC explicitly quantify the achievable performance and include the dynamics and transfer capacity of the transmission network [21]. The dynamics of dVOC in  $\alpha\beta$ -coordinates are represented by

$$\dot{\hat{v}} = \omega^* J_2 \hat{v} + \eta \left( K \hat{v} - R_2(\kappa) i + \frac{\alpha}{v^{*2}} (v^{*2} - \|\hat{v}\|^2) \hat{v} \right), \quad (15)$$

where  $\hat{v} = [\hat{v}_{\alpha} \ \hat{v}_{\beta}]^T$  is the reference voltage,  $i = [i_{\alpha} \ i_{\beta}]^T$  is current injection of the converter, the angle  $\kappa := \tan^{-1}(l\omega^*/r)$  models the network inductance to resistance ratio, and  $\eta, \alpha$  are positive control gains. Furthermore we have

$$R_2(\kappa) := \begin{bmatrix} \cos \kappa & -\sin \kappa \\ \sin \kappa & \cos \kappa \end{bmatrix}, K := \frac{1}{v^{*2}} R_2(\kappa) \begin{bmatrix} p^* & q^* \\ -q^* & p^* \end{bmatrix},$$

where  $R_2(\kappa)$  is the 2-D rotation by  $\kappa$ . As shown in [21] the dynamics (15) reduce to a harmonic oscillator if phase synchronization is achieved (i.e.,  $K \hat{v} - R_2(\kappa) i = 0$ ) and  $\|\hat{v}\| = v^*$  (i.e.,  $(v^{*2} - \|\hat{v}\|^2) \hat{v} = 0$ ). Rewriting (15) in polar coordinates for an inductive network (i.e.,  $\kappa = \pi/2$ ) reveals the droop characteristics (see [20]–[22]) of dVOC as

$$\dot{\theta} = \omega = \omega^* + \eta \left( \frac{p^*}{v^{*2}} - \frac{p}{\|\hat{v}\|^2} \right), \quad (16a)$$

$$\|\dot{\hat{v}}\| = \eta \left( \frac{q^*}{v^{*2}} - \frac{q}{\|\hat{v}\|^2} \right) \|\hat{v}\| + \frac{\eta \alpha}{v^{*2}} (v^{*2} - \|\hat{v}\|^2) \|\hat{v}\|. \quad (16b)$$

In other words, for a high voltage network and near the nominal steady state (i.e.,  $v^* \approx \|\hat{v}\|$ ) the relationship between frequency and active power resemble that of standard droop control given in (8) with  $d_{\omega} = \eta/v^{*2}$ . Moreover, when choosing the control gain  $\alpha$  to obtain post-fault voltages consistent with the other control algorithms described above, the first term in (16b) is negligible and (16b) reduces to the voltage regulator  $\|\dot{\hat{v}}\| \approx -2\eta\alpha(\|\hat{v}\| - v^*)$  near the nominal steady state.

## IV. NETWORK CASE STUDY

In this section we present a comparison study of grid-forming control techniques in the presence of synchronous machines. In the forthcoming discussion, we use the test system shown in Figure 3. The parameters and control gains are given in Table I. The implementation in Simulink is available online [31].

Each GFC in Figure 3 consists of a reduced-order model (1) of the modular system illustrated in Figure 2 with 100 modules per unit. The parameters of the module components - two identical 500 kVA converters and one 1.6 MVA transformer - correspond to those of commercially available devices. To avoid phase-locked loop (PLL) based frequency measurement, we use the mechanical frequency of the synchronous machine to evaluate the post-disturbance system frequency. Lastly, we assume that the system is in steady-state at  $t = 0$ .

### A. Performance Metrics Definition

We adopt the maximum frequency deviation (i.e., frequency nadir/zenith) and RoCoF as performance metrics [1], [32]

$$\|\Delta\omega\|_{\infty} := \max_{t \geq t_0} |\omega^* - \omega(t)|, \quad (17a)$$

$$|\dot{\omega}| := \frac{|\omega(t+T) - \omega(t)|}{T}, \quad (17b)$$

where  $t_0 > 0$  is the time when the disturbance is applied to the system, and  $T > 0$  is the RoCoF calculation window. In this work, we use  $T = 250$ ms, which is in line with values suggested for protection schemes (see [33, Table 1]). Dividing the metrics (17) by the size of the magnitude of the disturbance results in a measure of the systems disturbance amplification.

### B. Test Network Configuration and Tuning Criteria

In order to study the performance of the control approaches introduced in Section III, we apply the same strategy (with identical tuning) for both converters (i.e., at nodes 2 and 3 in Figure 3), resulting in four different SM-GFC paired models. As a benchmark, we also consider an all machine system with three identical SMs (i.e., at nodes 1-3). Selecting fair tuning

TABLE I: Parameters used for the case study.

IEEE 9-bus test system base values					
$s_b$	100 MVA	$v_b$	230 kV	$\omega_b$	2 $\pi$ 50 rad/s
MV/HV transformer					
$s_r$	210 MVA	$v_1$	13.8 kV	$v_2$	230 kV
$r_1 = r_2$	0.0027 pu	$l_1 = l_2$	0.08 pu	$r_m = l_m$	500 pu
LV/MV transformer					
$s_r$	1.6 MVA	$v_1$	1 kV	$v_2$	13.8 kV
$r_1 = r_2$	0.0073 pu	$l_1 = l_2$	0.018 pu	$r_m, l_m$	347, 156 pu
synchronous machine					
$s_r$	100 MVA	$v_r$	13.8 kV	$\omega_b$	2 $\pi$ 50 rad/s
$H$	3.7 s	$d_p$	1 %	$\tau_g$	5 s
voltage source converter					
$s_r$	500 kVA	$g_{dc}, c_{dc}$	0.83, 0.008 $\Omega^{-1}$ , F	$v_{dc}^*, v^*$	2.44, 1 kV
$r$	0.001 $\Omega$	$l$	200 $\mu$ H	$c$	300 $\mu$ F
$n$	100	$\tau_{dc}$	50 ms	$i_{max}$	1.2 pu
AC current, AC voltage, and DC voltage control					
$k_{pv}, k_{iv}$	0.52, 232.2	$k_{pi}, k_{ii}$	0.73, 0.0059	$k_{dc}$	$1.6 \times 10^3$
droop control					
$d_{\omega}$	2 $\pi$ 0.05 rad/s	$\omega^*$	2 $\pi$ 50	$k_p, k_i$	0.001, 0.5
virtual synchronous machine (VSM)					
$D_p$	10 $^5$	$J$	2 $\times 10^3$	$k_p, k_i$	0.001, 0.0021
matching control					
$k_{\theta}$	0.12	$k_{dc}$	1.6 $\times 10^3$	$k_p, k_i$	0.001, 0.5
dispatchable virtual oscillator control (dVOC)					
$\eta$	0.021	$\alpha$	6.66 $\times 10^4$	$\kappa$	$\pi/2$

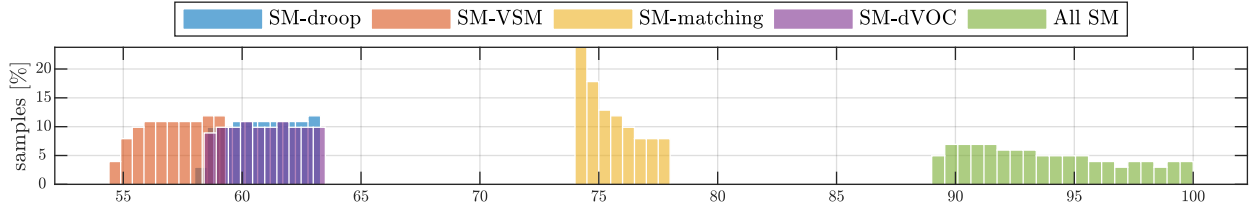


Fig. 4: Normalized distribution of the RoCoF  $|\dot{\omega}_i|/|\Delta p_i|$  of the synchronous machine frequency at node 1 for load disturbances  $\Delta p_i$  ranging from 0.2 p.u. to 0.9 p.u. at node 7.

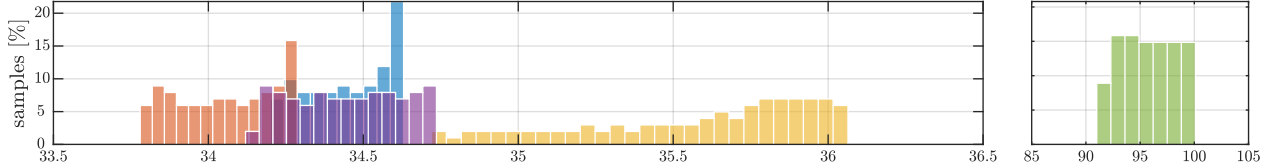


Fig. 5: Normalized distribution of the nadir  $\|\Delta\omega_i\|_\infty/|\Delta p_i|$  of the synchronous machine frequency at node 1 for load disturbances  $\Delta p_i$  ranging from 0.2 p.u. to 0.9 p.u. at node 7.

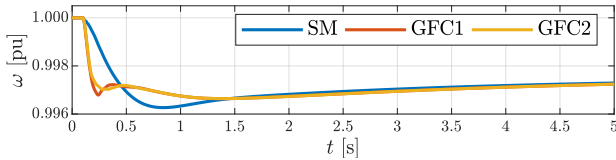


Fig. 6: Frequency of the system with two VSMs after a 0.75 pu load increase. The converters quickly synchronize with each other and then slowly synchronize with the machine.

criteria for the different control strategies is a challenging task. For this study, we tune the control parameters such that all generation units exhibit identical proportional load sharing behavior, i.e.,  $d_p$  in (4),  $d_\omega$  in (8),  $D_p$  in (10),  $k_{dc}$  in (7), and  $\eta$  in (15) are computed such that the steady-state frequency deviation for a given change in network load is identical (cf. [5]). The reader is referred to [5], [10], [20] for more details on the load-sharing capabilities of the aforementioned control solutions. Moreover, the control gains in (9), (12), (14) and (16b) are selected to regulate the AC voltage at approximately equal time-scales.

### C. Impact of Grid-Forming Control on Frequency Metrics

In this section we test the system behavior for different load disturbances  $\Delta p_i$ . The network base load  $p_l$  is constant and uniformly distributed between nodes 5, 7 and 9 while  $\Delta p_i$  is only applied at node 7. For each disturbance input we calculate  $\|\Delta\omega_i\|_\infty$  and  $|\dot{\omega}_i|$  for the SM at node 1 and normalize these quantities by dividing by  $|\Delta p_i|$ . Figures 4 and 5 illustrate the distribution of system disturbance input/output gains associated with introduced frequency performance metrics. Note that the network base load  $p_l$  is 2 pu and the elements of the load disturbance sequence  $\Delta p_i \in [0.2, 0.9]$ ,  $i = 1, \dots, 100$  are uniformly increasing by 0.007 pu starting from  $p_1 = 0.2$  pu.

Figures 4 and 5 suggest that, regardless of the choice of control strategy, the presence of grid-forming converters improves the metrics compared to the all-SM system. This possibly surprising observation can be explained by the fast response of converters compared to the slow turbine dynamics, i.e.,  $\tau_g$  in (4) is larger than  $\tau_{dc}$  in (2). Because of this,

the converters reach frequency synchronization at a faster time-scale and then synchronize with the SM (see Figure 6). Overall, for any given disturbance input, the converters are able to react faster than the SM and the remaining power imbalance affecting the SM is smaller than in the all-SM system. This result highlights that the fast response of GFCs should be exploited instead of designing the controls of a converter (fast physical system) to emulate the slow response of synchronous machines [1].

We observe that droop control and dVOC exhibit very similar performance confirming the droop-like behavior of dVOC in predominately inductive networks (see (16)). Moreover, the difference between droop control and VSM arises from the inertial (derivative control) term in (10) and the RoCoF is considerably higher when using matching control. This can be explained by the fact that VSM, droop control, and dVOC ignore the DC voltage and aggressively regulate AC quantities to reach angle synchronization, thus requiring higher transient peaks in DC current to stabilize the DC voltage (see Section IV-D). Although improving RoCoF, this approach can lead to instability if the converter is working close to the rated power of the DC source, as shown in the next section. On the other hand, matching control regulates the DC link voltage both through the DC source and by adjusting its AC signals.

Last but not least, we selected the RoCoF calculation window according to the guideline [33], which accounts for noise and possible oscillations in the frequency signal. However, these guidelines were derived for a power system fully operated based on synchronous machines. Given that grid-forming converters introduce faster dynamics, machines are expected to reach the frequency nadir faster. Hence, a smaller RoCoF windows might need to be considered in a low-inertia power system to properly assess system performance. We note that the performance of the different grid-forming control strategies shown in Figure 4 and 5 is sensitive to the tuning of control gains and choice of RoCoF computation window. However, due to the comparably slow response of conventional generation technology the performance improvements for the system with grid-forming converters over the all-SM system persists for a wide range of parameters. Moreover, using

comparable tuning (see Section IV-B) the differences between the different grid-forming techniques observed in this section are expected to remain the same.

#### D. Instability Behavior – Large Load Disturbance

In this subsection we analyze the response of the grid-forming converters to large disturbances when the DC source is working close to its maximum rated values. To begin with, we set the network base load  $p_l$  and load change  $\Delta p$  to 2.25 and 0.75 pu respectively. Figure 7 shows the DC voltage and delayed DC current (i.e., before the saturation (3)) of the converter at node 2. Considering the base loading and large disturbance magnitude (which rarely occurs in transmission systems), it is interesting to observe that all controls remain stable. We now increase  $\Delta p$  to 0.9 pu (i.e., a total network load after the disturbance of 3.15 pu) which is equally shared by the machine and the converters. We expect a post-disturbance converter power injection of 1.05 pu and  $i_{dc}$  close to the DC current limit  $i_{max} = \pm 1.2$  pu. Figure 8 shows the DC voltage and delayed DC current before saturation for the converter at node 2 for a load increase of  $\Delta p = 0.9$  pu. For sufficiently large disturbance magnitude,  $i_{dc}^*$  and consequently  $i_{\tau}$  exceed the current limit, i.e., the DC current  $i_{dc} = i_{max}$  is saturated. We observe that the VSM, droop control, and dVOC fail to converge to a stable post-event equilibrium if the DC source is saturated for a prolonged time. In contrast, the GFCs controlled by matching reach a stable post-event equilibrium. Pinpointing the underlying cause of instability is not straightforward. For the VSM and converters controlled by droop control and dVOC the DC-link capacitor discharges to provide  $i_{\tau} - i_{max}$  (i.e., the portion of current demand which is not provided due to the saturation (3)). For droop control and the VSM this results in a collapse of the DC voltage. When the DC voltage drops below a certain limit - tripping the converter in practice - the AC voltage collapses and consequently the reactive power diverges far off the practical limits. This is followed by a similar instability behavior for active power. Because dVOC decreases its power injection if the voltage is low (i.e.,  $\|v\|^2 < v^{*2}$  and  $p$  and  $q$  resulting from (15) are lower) the DC voltage does not collapse immediately. Nonetheless, dVOC cannot reach a synchronous solution and becomes unstable because the DC current is limited.

Reducing the AC voltage control gains in (9) and (11), i.e., enforcing stronger DC-AC dynamics time-scale separation, stabilizes all GFCs but less accurate tracking of the reference voltage  $\hat{v}$ . Additionally, it has been observed that removing the inner voltage and current tracking loops (5)-(6), i.e., using  $\hat{v}$  directly to obtain the modulation, stabilizes all three strategies. This supports the argument made in [13] that removing the inner loops increases the bandwidth of the controller and can result in increased performance. However, we remark that these ad hoc remedies by no means guarantee stability for larger disturbances or different converter and network parameters. Finally, it has been reported that limiting the AC current also destabilizes droop control [34].

Remarkably, matching control is able to render the system stable by exhibiting a mode switching behavior from grid-forming to constant current source mode resembling a similar

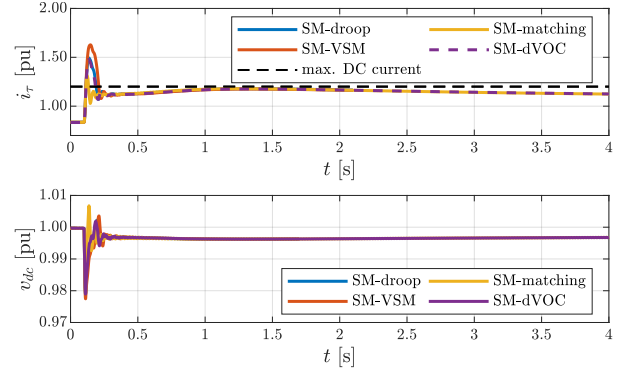


Fig. 7: DC current demand of the converter at node 2 (top) and its DC voltage (bottom) after a 0.75 pu load disturbance.

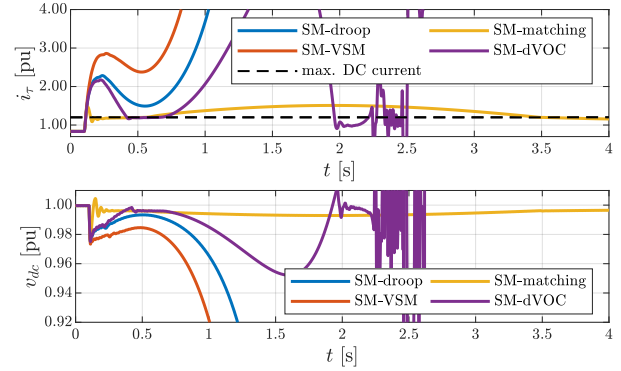


Fig. 8: DC current demand of the converter at node 2 (top) and its DC voltage (bottom) after a 0.9 pu load disturbance.

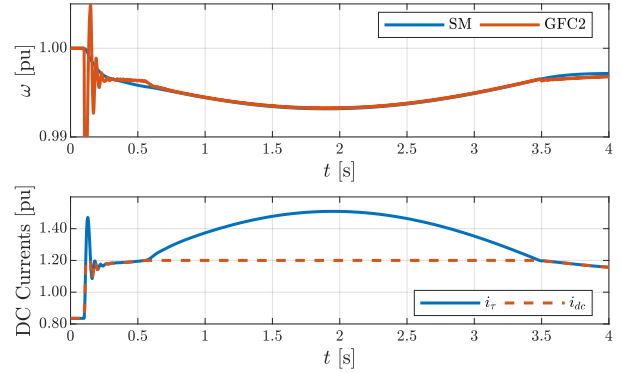


Fig. 9: Frequency (equal to DC voltage in pu) of the converter (using matching control) at node 2 and SM after a 0.9 pu load disturbance (top) and the DC current demand and saturated DC current (bottom).

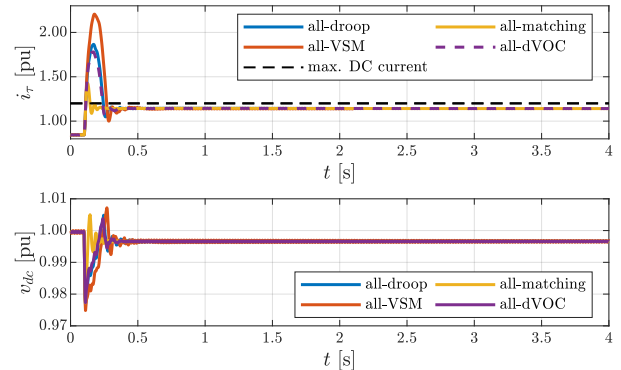


Fig. 10: DC current demand (top) and DC voltage (bottom) after a 0.9 pu load disturbance in an all-GFC system.

behavior as grid-following converters. In other words, even though the converter does not measure frequency explicitly, it follows the system frequency (see Figure 9). In contrast to the other techniques matching control succeeds to stabilize DC voltage despite saturation of the DC source. From a circuit-theoretic point of view this is only possible if the sum of the AC power injection and filter losses equals the approximately constant DC power inflow  $v_{dc}i_{max}$ . The converter can only inject constant AC power into the network if its angle difference with respect to the remaining devices in the network is constant. In the presence of the slow SM angle and frequency dynamics this implies that the GFCs need to synchronize to the SM (and with each other) so that the relative angle  $\theta_{GFC} - \theta_{SM} = \theta_{max}$  is constant.

This synchronization is achieved through the DC voltage imbalance, i.e., as long as the DC voltage deviates from its nominal value matching control adjusts its voltage angle (see (13)). In particular, the brief initial frequency transient (after the DC current reaches its limit) shown in Figure 9 balances the power flowing in and out of the DC capacitor and results in an angle difference to the SM of  $\theta_{max}$ . Overall, this results in stability of DC link voltage (i.e., by (13)  $v_{dc} = \omega_{GFC}/\eta = \omega_{SM}/\eta$ ). The matching controlled converter switches its behavior as soon as  $i_\tau$  exceeds the limit at approximately  $t = 0.5s$  in Figure 9. At around  $t = 3.5s$ , the machine output power is sufficiently close to its steady-state value,  $i_{dc}^*$  and  $i_\tau$  return to below the limit  $i_{max}$ , and the matching controlled converter recovers its DC voltage and frequency regulation capability and grid-forming dynamics. This behavior of matching control has been observed also for larger disturbance magnitudes. The nature of matching control - which accounts for the DC side dynamics while regulating the AC dynamics - results in increased robustness with respect to large disturbances. In contrast, droop control, dVOC, and the VSM implicitly assume that the DC and AC side are two independent systems and that can be regulated independently. This assumption is only justified under benign conditions and does not hold for large disturbances. As a consequence droop control, dVOC, and the VSM all exceed the limitations of the DC source for large disturbances and become unstable.

We observe the same instability of droop control, VSM, and dVOC when the test system contains one GFC and two SMs, i.e., the instability cannot be prevented by adding more inertia to the system. Figure 10 shows the DC current demand  $i_\tau$  (i.e., before saturation) and DC voltage in an all-GFC system for a load increase of  $\Delta p = 0.9$  pu. The GFCs quickly synchronize to the post-event steady state, which does not exceed the maximum DC current, saturate the DC source for only approximately 200ms, and remain stable. In contrast, in the system with two GFCs and one SM, the SM does not reach its increased post-event steady-state power injection for several seconds. During this time the response of droop control, VSM, and dVOC results in a power injection that exceeds the limits of the DC source and collapses the DC voltage. This highlights that the interaction of the fast GFC dynamics and slow SM dynamics contributes to the instability shown in Figure 8.

### E. Loss of Synchronous Machine Scenario

In this section, we study the response of grid-forming converters when disconnecting the synchronous machine at node 1, that is, the system turns into an all-GFCs network. The implications of such a contingency are threefold. First, the power injected by the machine, which partially supplies the base load, is no longer available. Second, the stabilizing dynamics associated with the machine's governor, AVR, and PSS are removed from the system. Third, the slow dynamics of the SM no longer interact with the fast dynamics of the GFCs. For this test, we set the base load to 2.1 pu, and the turbine and converter power set-points are set to 0.6 and 0.75 pu respectively. Note that when the SM at node 1 is disconnected, the converters increase their power output according to the power sharing behavior inherent to all four grid forming controls. The resulting increase in the converter power injection to roughly 1.05 pu is similar to the load disturbance scenario used to study the unstable behavior of droop control, the VSM, and dVOC in the previous section. Figure 11 shows  $i_\tau$  and  $v_{dc}$  for the converter at node 2. Although the disturbance magnitude affecting the converters is similar to the one in studied in previous subsection, all GFCs remain stable after the loss of the SM. In particular, due to the absence of the slow turbine dynamics and fast synchronization of the converters  $i_\tau$  is only above the limit  $i_{max}$  for around 50ms while it remains above the limit for a prolonged period of time in Figure 8. This again highlights the problematic interaction between the fast response of the GFCs and the slow response of the SM. We stress that this adverse interaction is not resolved by increasing the inertia in the system (see the discussion in the previous subsection). While the synchronous machine perfectly meets classic power system control objectives on slower time scales, the dominant feature of GFCs is their fast response. However, the fast response of GFCs can also result in unforeseen interactions with other parts of the system such as the slow SM response (shown here), line dynamics (see [21], [29]), and line limits [35]. For instance, during a recent separation event in Australia the rapid response of a battery energy storage system provided a valuable contribution frequency stabilization but also contributed to tripping a line and islanding an area [35, p. 67]. Therefore, we expect to observe further adverse interactions in future studies related

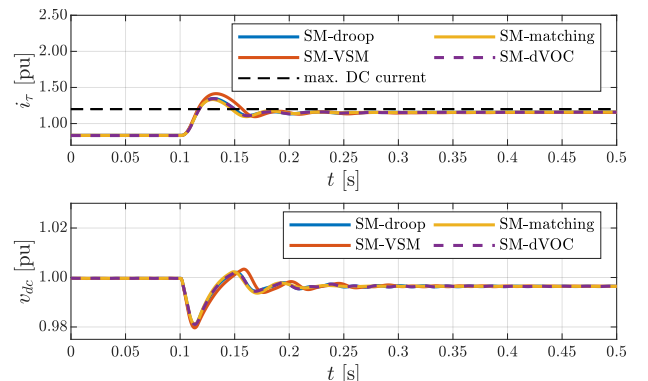


Fig. 11: DC current demand (top) and DC voltage (bottom) of the converter at node 2 after the loss of the SM at node 1.

to low-inertia power system.

## V. SUMMARY AND FURTHER WORK

In this paper we provided an extensive review of different grid-forming control techniques. Subsequently, we used the IEEE 9-bus system to compare the performance of different techniques and their interaction with synchronous machines. First, we showed that replacing synchronous machines with GFCs improves frequency stability metrics compared to the original all-machine system. Next, simulating a large load disturbance we showed that some GFCs become unstable when the DC source current is limited for a prolonged time. In contrast, matching control exhibits a change in operating mode from grid-forming to constant current source mode and remains stable. We investigated the behavior of GFCs in response to the loss of a synchronous machine and highlighted a potentially destabilizing interaction between the fast synchronization of GFCs and the slow response of SMs. We emphasize that the impact of the DC dynamics on system stability needs to be studied using more detailed DC energy source models. Furthermore, investigating model reduction techniques for large-scale grid-forming converter systems is an interesting yet not thoroughly studied aspect of the problem. Lastly, future work will analyze the switching behavior of matching control and blending of the different control strategies into a controller that achieves their complementary benefits.

## REFERENCES

- [1] F. Milano, F. Dörfler, G. Hug, D. J. Hill, and G. Verbič, "Foundations and Challenges of Low-Inertia Systems," in *Power Systems Computation Conference (PSCC)*, 2018.
- [2] B. Kroposki, B. Johnson, Y. Zhang, V. Gevorgian, P. Denholm, B. M. Hodge, and B. Hannegan, "Achieving a 100% Renewable Grid: Operating Electric Power Systems with Extremely High Levels of Variable Renewable Energy," *IEEE Power Energy Mag.*, vol. 15, no. 2, pp. 61–73, 2017.
- [3] P. Kundur, *Power system stability and control*. McGraw-Hill, 1994.
- [4] G. Denis, T. Prevost, M. Debry, F. Xavier, X. Guillaud, and A. Menze, "The Migrate project: the challenges of operating a transmission grid with only inverter-based generation. A grid-forming control improvement with transient current-limiting control," *IET Renewable Power Generation*, vol. 12, no. 5, pp. 523–529, 2018.
- [5] A. Tayyebi, F. Dörfler, F. Kupzog, Z. Miletic, and W. Hribernik, "Grid-Forming Converters – Inevitability, Control Strategies and Challenges in Future Grid Applications," in *CIREP Workshop*, 2018.
- [6] "High Penetration of Power Electronic Interfaced Power Sources (HPoPEIPS) ENTSO-E Guidance document for national implementation for network codes on grid connection," ENTSO-E, Tech. Rep., 2017.
- [7] M. Chandorkar, D. Divan, and R. Adapa, "Control of parallel connected inverters in standalone AC supply systems," *IEEE Trans. Ind. Appl.*, vol. 29, no. 1, pp. 136–143, 1993.
- [8] J. W. Simpson-Porco, F. Dörfler, and F. Bullo, "Synchronization and power sharing for droop-controlled inverters in islanded microgrids," *Automatica*, vol. 49, no. 9, pp. 2603–2611, 2013.
- [9] B. Johnson, M. Rodriguez, M. Sinha, and S. Dhople, "Comparison of virtual oscillator and droop control," in *IEEE Workshop on Control and Modeling for Power Electronics (COMPEL)*, 2017.
- [10] S. D'Arco, J. A. Suul, and O. B. Fosso, "A Virtual Synchronous Machine implementation for distributed control of power converters in SmartGrids," *Electric Power Systems Research*, vol. 122, pp. 180–197, 2015.
- [11] H. Bevrani, T. Ise, and Y. Miura, "Virtual synchronous generators: A survey and new perspectives," *International Journal of Electrical Power & Energy Systems*, vol. 54, pp. 244–254, 2014.
- [12] Q. C. Zhong and G. Weiss, "Synchronverters: Inverters That Mimic Synchronous Generators," *IEEE Trans. Ind. Electron.*, vol. 58, no. 4, pp. 1259–1267, 2011.
- [13] Q. Zhong, P. Nguyen, Z. Ma, and W. Sheng, "Self-synchronized synchronverters: Inverters without a dedicated synchronization unit," *IEEE Trans. Power Electron.*, vol. 29, no. 2, pp. 617–630, 2014.
- [14] I. Cvetkovic, D. Boroyevich, R. Burgos, C. Li, and P. Mattavelli, "Modeling and control of grid-connected voltage-source converters emulating isotropic and anisotropic synchronous machines," in *IEEE Workshop on Control and Modeling for Power Electronics (COMPEL)*, 2015.
- [15] L. Huang, H. Xin, Z. Wang, K. Wu, H. Wang, J. Hu, and C. Lu, "A virtual synchronous control for voltage-source converters utilizing dynamics of DC-link capacitor to realize self-synchronization," *IEEE Trans. Emerg. Sel. Topics Power Electron.*, vol. 5, no. 4, pp. 1565–1577, 2017.
- [16] C. Arghir, T. Jouini, and F. Dörfler, "Grid-forming control for power converters based on matching of synchronous machines," *Automatica*, vol. 95, pp. 273–282, 2018.
- [17] S. Curi, D. Groß, and F. Dörfler, "Control of low-inertia power grids: A model reduction approach," in *IEEE Conference on Decision and Control (CDC)*, 2017, pp. 5708–5713.
- [18] B. B. Johnson, S. V. Dhople, J. L. Cale, A. O. Hamadeh, and P. T. Krein, "Oscillator-Based Inverter Control for Islanded Three-Phase Microgrids," *IEEE J. Photovolt.*, vol. 4, no. 1, pp. 387–395, 2014.
- [19] M. Sinha, F. Dörfler, B. B. Johnson, and S. V. Dhople, "Uncovering Droop Control Laws Embedded Within the Nonlinear Dynamics of Van der Pol Oscillators," *IEEE Trans. Control Netw. Syst.*, vol. 4, no. 2, pp. 347–358, 2017.
- [20] M. Colombino, D. Groß, J. Brouillon, and F. Dörfler, "Global phase and magnitude synchronization of coupled oscillators with application to the control of grid-forming power inverters," *IEEE Trans. Autom. Control*, 2019.
- [21] D. Groß, M. Colombino, J.-S. Brouillon, and F. Dörfler, "The effect of transmission-line dynamics on grid-forming dispatchable virtual oscillator control," *arXiv:1802.08881*, 2018.
- [22] G. Seo, I. Subotic, B. Johnson, M. Colombino, D. Groß, and F. Dörfler, "Dispatchable virtual oscillator control for decentralized inverter-dominant power systems – analysis of droop characteristic and verification," in *Applied Power Electronics Conference (APEC)*, 2018.
- [23] A. H. Etemadi, E. J. Davison, and R. Iravani, "A Decentralized Robust Control Strategy for Multi-DER Microgrids – Part I: Fundamental Concepts," *IEEE Trans. Power Del.*, vol. 27, no. 4, pp. 1843–1853, 2012.
- [24] T. Qoria, F. Gruson, F. Colas, X. Guillaud, M. Debry, and T. Prevost, "Tuning of cascaded controllers for robust grid-forming voltage source converter," in *Power Systems Computation Conference (PSCC)*, 2018.
- [25] V. Purba, S. V. Dhople, S. Jafarpour, F. Bullo, and B. B. Johnson, "Reduced-order structure-preserving model for parallel-connected three-phase grid-tied inverters," in *IEEE Workshop on Control and Modeling for Power Electronics (COMPEL)*, 2017.
- [26] "Matlab/Simulink SimPowerSystem synchronous machine model," MathWorks, Inc, model documentation, mathworks.com.
- [27] *IEEE Recommended Practice for Excitation System Models for Power System Stability Studies*, IEEE Std. 421.5, 2016.
- [28] R. D. Zimmerman, C. E. Murillo-Sanchez, and R. J. Thomas, "Matpower: Steady-state operations, planning, and analysis tools for power systems research and education," *IEEE Trans. Power Syst.*, vol. 26, no. 1, pp. 12–19, 2011.
- [29] P. Vorobev, P. Huang, M. A. Hosani, J. L. Kirtley, and K. Turitsyn, "High-fidelity model order reduction for microgrids stability assessment," *IEEE Trans. Power Syst.*, vol. 33, no. 1, pp. 874–887, 2018.
- [30] U. Markovic, O. Stanojev, E. Vrettos, P. Aristidou, and G. Hug, "Understanding stability of low-inertia systems," *enrXiv preprint*, 2019, <http://enrXiv.org/jwzrq>.
- [31] A. Tayyebi, D. Groß, and A. Anta, "GridFormingConverters: Implementation of grid-forming control techniques in IEEE 9-bus system," Git repository, 2019, <https://github.com/ATayyebi/GridFormingConverters>.
- [32] B. K. Poolla, D. Gross, and F. Dörfler, "Placement and implementation of grid-forming and grid-following virtual inertia and fast frequency response," *IEEE Trans. Power Syst.*, 2019.
- [33] RG-CE System Protection & Dynamics Sub Group, "Frequency measurement requirements and usage," ENTSO-E, Tech. Rep., 2018.
- [34] H. Xin, L. Huang, L. Zhang, Z. Wang, and J. Hu, "Synchronous instability mechanism of P-f droop-controlled voltage source converter caused by current saturation," *IEEE Trans. Power Syst.*, vol. 31, no. 6, pp. 5206–5207, 2016.
- [35] "Final report - Queensland and South Australia system separation on 25 august 2018," AEMO, Tech. Rep., 2019.